THE JOURNAL OF PHYSICAL CHEMISTRY C
A JOURNAL OF THE AMERICAN CHEMICAL SOCIETY

pubs.acs.org/JPCC

Article

Molecular Bond Engineering and Feature Learning for the Design of Hybrid Organic–Inorganic Perovskite Solar Cells with Strong Noncovalent Halogen–Cation Interactions

Johannes L. Teunissen* and Fabiana Da Pieve

Cite This: J. Phys. Chem. C 2021, 125, 25316–25326

Read Online

ACCESS | Metrics & More | Article Recommendations | Supporting Information

ABSTRACT: Hybrid organic–inorganic perovskites are exceedingly interesting candidates for new solar energy technologies for both ground-based and space applications. However, their large-scale production is hampered by the lack of long-term stability, mostly associated with ion migration. The specific role of noncovalent bonds in contributing to the stability remains elusive, and in certain cases controversial. Here, we perform an investigation on a large perovskite chemical space via a combination of first-principles calculations for the bond strengths and the recently developed sure independent screening and sparsifying operator (SISSO) algorithm. The latter is used to formulate mathematical descriptors that, by highlighting the importance of specific noncovalent molecular bonds, can guide the design of perovskites with suppressed ion migration. The results unveil the distinct nature of different noncovalent interactions, with remarkable differences compared to previous arguments and interpretations in the literature on the basis of smaller chemical spaces. In particular, we clarify the origin of the higher stability offered by formamidinium compared to methylammonium, which shows to be different from previous arguments in the literature, and the reasons for the improved stability given by the halogen F and explain the exceptional case of overall stronger bonds for guanidiunium. Within the stability boundaries given by the Goldschmidt factor, the found descriptors give an all-in-one picture of noncovalent interactions which provide more stable configurations, also including interactions other than H bonds. Such descriptors are more informative than previously used quantities and can be used as a universal input to better inform new machine learning studies.

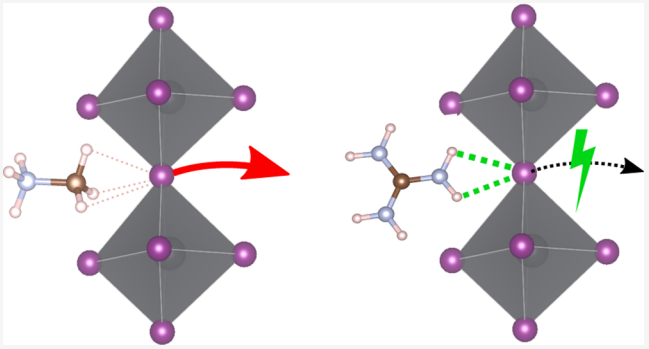

INTRODUCTION

Hybrid organic–inorganic perovskite (HOIP)-based solar cells are emerging as a new opportunity for a paradigm shift in solar cell technology for both Earth-based[1] and space applications.[2−4] On the Earth, due to the increasing demand for clean energy resources, the rapidly evolving high power conversion efficiency (PCE)[5,6] of HOIPs and their relatively low-cost fabrication[7] make them potential candidates for a step-change approach to harvest solar energy. For space missions, HOIPs qualify as the best candidates for extremely lightweight,[3] flexible, and radiation-resistant solar panels.[8−12] Either for missions in the Earth's vicinity or deep space, these systems show potential for reducing the weight at launch, for broad absorption that matches the operating conditions at both Earth and Martian orbits, and for fabrication via 3D printing techniques, considered as necessary for on-mission manufacturing.[3,13] For stays on the Moon or Mars, these systems offer the potential for autonomous roll-out of solar arrays for extraterrestrial surface deployments.

HOIPs comprise a negatively charged lead-halide inorganic skeleton with a composition of ABX_3, where B is a metal cation (Sn^{2+} or Pb^{2+}), X is a halide anion (I^-, Br^-, and/or Cl^-) and A is a monovalent positively charged organic cation, such as methylammonium ($MA = CH_3NH_3X^+$, where X = I, Br, or Cl) or formamidinium [$FA = CH(NH_2)_2^+$]. The organic cation plays a fundamental role for the stability of the structure. Perovskite materials have excellent optical and electrical properties for solar cell applications, such as strong light absorption,[14,15] steep optical absorption edge,[16] band gap tuning,[17] high charge carrier mobility,[18−20] possible polaron-protected transport properties[21−23] (although debated[24]), low exciton binding energy,[25,26] and long charge-carrier diffusion lengths and carrier lifetimes.[20,27,28]

The recent steep increase in the PCE of perovskite solar cells makes them the fastest advancing solar technology. Never-

Received: September 3, 2021
Revised: October 19, 2021
Published: November 4, 2021

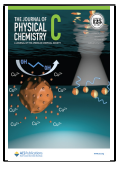

theless, despite the many advantages, the progress in large-scale applications and production of HOIPs is hampered by instability issues. Indeed, HOIPs suffer from structural instabilities induced by air, moisture,[29] UV light,[30−32] and heat, causing the perovskite solar cells to have a particularly low lifetime. Intrinsic instability causing unavoidable decomposition with time has also been reported.[31] The instability is mainly caused by a relatively weak cohesion between the organic cation and the inorganic octahedra and predominantly by the low energy barriers for the migration of halide anions and organic cations, with halide migration being the most prevalent.[33−37] Nevertheless, the (short-term) performance of HOIP-based solar cells is considerably defect tolerant. Density functional theory (DFT) calculations based on hybrid functionals with spin-orbit coupling have shown that the majority of the defects induce only shallow defect states near the band edges[38,39] and that although iodine interstitials create deep levels in the gap of $MAPbI_3$,[40,41] these only leave short-living hole traps.[34,42] Still, there remain unwanted effects in the carrier dynamics, $I-V$ hysteresis, and chemical degradation of the HOIP and at the interfaces with the charge transport layers. Ion migration has also been reported to greatly accelerate charge carrier losses[43] and, in large scale, also to cause phase segregation.[44]

A tremendous experimental effort has been devoted to overcome the above shortcomings of HOIPs, though intrinsic improvements (mostly by changing the stoichiometry) or extrinsic improvements (such as encapsulation) reduce exposure to degradation factors. For example, intrinsic improvements consist in changing the amount of or mixing different organic cations, such as through insertion of excess or combined MA/FA,[45−47] introducing small amounts of larger organic molecules,[48] inserting guanidinium,[47,49] changing the amount of iodine,[50] or mixing different halides[51] via mixed-cation systems (e.g., by including inorganic cations such as rubidium or caesium)[52] through doping for lattice strain relaxation-induced suppression of halide vacancies,[53] multi-vacancy defect passivation,[54] lower-dimensional HOIPs or additional layers,[55] and chemical bond modulation by tuning the bond strength of the additives.[56,57]

Halogen migration can be mitigated by increasing the binding strength with the organic cations.[50,58,59] The organic cation binds strongly with the halogen anions via hydrogen bonding, and when the cation has double bonds, it binds also via $\pi\cdots$anion binding.[60] Several papers have shown that in $MAPbI_3$, only the N−H···I hydrogen bonds are important,[61−63] although recently it was advocated[62] that non-covalent interactions other than N−H···I, such as C−H···I and N/C···I, are also of importance. Nonetheless, neither computational nor experimental methods can easily deconvolute the individual contributions to the energetics of the bonds as a continuous merge between the hydrogen bond with van der Waals interactions and ionic and covalent bonds,[64] and despite the tremendous efforts, the unique properties of metal halides perovskites remain elusive.

In this work, we combine a first-principles analysis of bonds based on the quantum-theory-of-atoms-in-molecules (QTAIM)[65] with a feature learning analysis through the sure independence screening and sparsifying operator (SISSO) algorithm[66] on a large chemical space to untangle the contribution from different bond types and investigate the features that dominate in the relationship between the structural composition of the HOIPs and the X-cation binding strengths. The findings provide new insights into the role of different noncovalent interactions, with considerably different interpretations to previous arguments in the literature on the basis of some few specific cases, and can be used to guide the design of more stable cells by carefully tuning the chemical and compositional/structural properties for ion migration suppression.

THEORY AND COMPUTATIONAL DETAILS

QTAIM and DFT Calculations. In order to find the binding strengths, we combine the "Atoms in Molecules" theory[65] and the empirically established relationship between the properties of bond critical points (BCPs).[35,67] Within this theory, a bonding interaction is defined as a maximum electron density path (bond path) connecting two interacting atoms. Critical points (CPs) are points where the gradient of the electron density $\nabla\rho$ becomes zero. BCPs are those type of CPs where the density increases in one direction while it decreases in the plane perpendicular to that direction. Thus, a BCP is a saddle point in the charge density along the bond path. The existence of a BCP between the acceptor atom and the donating hydrogen, as well as the charge density properties at this point, defined the major criteria of the existence of an H bond. These BCPs are often found close to the midpoints of two atoms that have a bonding interaction, either covalent or noncovalent. The estimation of the bonding strength starts from the Abramov's formula[68] for the local kinetic energy density, G, given as

$$G = \frac{3}{10}(3\pi^2)^{2/3}\rho^{5/3} + \frac{1}{72}|\nabla\rho|^{-1} + \frac{1}{6}\nabla^2\rho \quad (1)$$

where ρ is the electron density. G correlates linearly with the bonding strength.[67] At the BCPs, the second term vanished since the gradient is zero. The presence of a BCP indicates that there is a charge accumulation between the two bonded nuclei.[69] The larger the density at the BCP, the stronger the interaction. Negative gradients indicate covalent bonds, while noncovalent interactions show small but positive gradients.[69]

Mata et al.[67] fitted the bond strengths versus G and found a relationship with the bond strength E as $E = 0.429G$ with a high correlation of $R^2 = 0.990$. The absolute values obtained for the bond strengths do depend on the level of theory,[70] but the interest of this work lies predominantly in the trends, and hence, only relative differences matter. There exists some criticism concerning the BCPs[71] as some cases exist where there is a bonding interaction without a BCP being present, most notably 1,2-ethanediol,[72] but these cases seem to occur seldom, and in our study, we did not find any absence of BCPs for cation−halogen bonding interactions, so we reasonably expect our trends to hold.

For all noncovalent interactions analyzed in this study between an organic cation and a halogen, there is a clear and strong power law correlation between the bond lengths and the density at the BCP. For an analysis of the density and gradients at the BCPs, see Supporting Information Section 4.

As our starting set of perovskite structures, we take the dataset as prepared and provided by Kim et al.[73] of 1346 HOIPs. From this dataset, we only select those 548 that have a perovskite structure that is roughly a cubic arrangement of the metal atoms with the halogens surrounding these metals connected via corner sharing octahedrals and the organic cation in the cavity thus created. Finally, as per chemical composition, we only take the most stable one, that is, the one

https://doi.org/10.1021/acs.jpcc.1c07295
J. Phys. Chem. C 2021, 125, 25316−25326

with the lowest atomization energy (the energy required to separate the molecular structure into individual atoms) resulting in a final set of 190 HOIPs. For some chemical compositions, the perovskite structure is not the most stable structure. However, in this paper, we are primarily interested in the binding strength under the condition that the structure is perovskite. When the structure is nonperovskite, the binding characteristics are completely different, and we cannot compare the binding strengths between different chemical compositions. For example, for many hydroxylammonium or hydrazinium compounds (like hydroxylammonium germanium fluoride), the most stable structure is not a perovskite. Although for a certain chemical composition, the perovskite structure might not be the most stable, it might still provide relevant insight on how to design structurally stable perovskites. Moreover, in real applications, one often uses a mixture of different organic cations (e.g., $MA_xFA_{(1-x)}PbI_3$), and for the mixed compound, the perovskite structure might well be stable.[74]

For each of the 190 HOIPs, the BCPs between the organic cation and the halogen are determined. In every perovskite structure, there are three symmetrically unique halogen positions. Each inorganic cavity, whose shape is approximately cubic (most generally a paralellepiped), has 12 halogens close to the midpoints of the cube edges and thus located approximately in the [002], [020], and [200] planes of the cavity. Each organic cation located in the approximately cubic cavity can bind maximally to 12 halogens, of which there are 3 sets of 4 halogens that belong to the same unique crystallographic position. We are mainly interested in those of the three halogens that has the lowest cation binding energy since the weakest bound halogen will be most prone to halogen migration. In this paper, we will call the total bond strength between a single organic cation and its neighboring halogens E_{total}. This bond strength is the sum of the contribution from the three unique halogen positions. The bond strength of the halogen with the lowest cation binding energy is called E_{minX}.

The HOIP dataset as prepared by Kim et al. uses 3 metals (Ge, Sn, and Pb), 4 halogens (F, Cl, Br, and I), and 16 organic cations giving 192 ($3 \times 4 \times 16$) unique chemical compositions. For each composition, multiple crystallographic structural conformations are present. In total, 1346 structures were obtained using a minima-hopping method[75] followed by a DFT-PAW structure optimization including van der Waals dispersion interactions via the vdW-DF2 functional[76] using VASP.[77] This dataset is open-source and can also be found on the NoMaD database.[78] The crystallographic information format (cif) files of the dataset were read using the pymatgen library.[79]

For the systems with a perovskite structure, we calculated the continuous symmetry measures for cubicity[80] of the metal atoms and found that for most of the HOIPs, the metals are arranged in an approximately cubic shape. The HOIPs with the highest deviations from cubic cells contained propylammonium or butylammonium cations (see the Supporting Information). For two chemical compositions, no perovskite structures are present in the dataset, being ammonium lead fluoride and hydroxylammonium tin bromide. Hence, in this paper, we study 190 instead of 192 structures. All electron densities were obtained with Quantum ESPRESSO 6.3[81] using the HSE06 functional[82] and norm-conserving scalar relativistic pseudopotentials.[82] The kinetic energy cutoff of the wavefunction was set at 80 Ry and the cutoff of the charge density to 320 Ry. The HSE06 functional is regularly used for HOIPs and is known to give good electronic and structural results, although band gaps are slightly overestimated.[35,73,83] A $5 \times 5 \times 5$ Monkhorst−Pack grid was used centered on the Γ point. The electron densities were evaluated at a $400 \times 400 \times 400$ grid, and the CPs were obtained using the Critic2 program.[84] The bond strengths presented in this work are based on the structures with the lowest atomization energies. However, HOIPs are particularly known to undergo subtle phase transitions. At lower temperatures, some symmetry breaking occurs changing the structure from cubic to tetragonal to orthorhombic. However, the cation−halogen interactions are not expected to be significantly different as they are not for MA, one of the most mobile cations.[85] Due to the corresponding differences in crystal packing, the orientation and bond lengths of the organic cation with the halogens will change. Nevertheless, the nature of the bonds and the ability of the organic cation to bind with the halogen anions will stay the same, and the observed trends stay the same as long as the structure is a perovskite (for a comparison of all 548 perovskite structures, see Supporting Information Section 2). Also, Varadwaj et al.[62] found that the binding characteristics stay the same for different cation orientations, although Lee et al.[63] found that the energy difference between two different orientations of the MA cation in $MAPbI_3$ might be 45 meV. Since we found that the total bond strength for $MAPbI_3$ is 413 meV, this means that the binding strength might change by around 10% depending on the cation orientation. Taking all of this into consideration, we believe that the results presented in this paper show valuable trends in the binding characteristics of different perovskite structures that can be extrapolated to other crystal packings, for example, those of mixed-cation or mixed-halogen HOIPs.

SISSO Algorithm. Following the calculation of all E_{total} and E_{minX}, we try to establish a connection between the bond strengths and the chemical structure via symbolic regression. Symbolic regression tries to find a mathematical expression of the input features that best fit the data. Here, we try to find an expression of structural features that best predicts the cation−halogen binding strengths. The particular algorithm used is called SISSO which is based on a compressed sensing technique (*vide infra*).[66,86−88] It starts from a set of single-valued elementary features called Φ_0. It then recursively applies some unary and binary mathematical operations to create new feature spaces called Φ_i with i being the number of times the mathematical operations are applied. It then iteratively applies the sure independence screening (SIS) and the sparsifying operator (SO) until the desired dimension is reached. SIS selects a subspace of Φ_i that has the highest correlation with the target property (in our case the binding strengths), and SO selects the best descriptor from the union of all subspaces selected by all previous SIS steps.[66]

In our case, we used SISSO to extract the most important structural features that dictate the cation-X binding strengths, thus elucidating what kind of structural composition is optimal for HOIPs with suppressed X-migration. The included unary operations are ($\square^2$, $\sqrt{\square}$, $\square^{-1}$, $|\square|$), and the included binary operators are (+, −, *,/). We also set a maximum to the descriptor complexity, thus limiting the number of mathematical operations. This prevents the loss of scientific interpretability as the higher complexity descriptors become too convoluted, and from a certain point, higher complexity

https://doi.org/10.1021/acs.jpcc.1c07295
J. Phys. Chem. C 2021, 125, 25316−25326

features do not give significantly better results. Setting the maximum complexity can be seen as a measure to prevent over-fitting.

We decided to only include features that can be derived directly from the given structure. No features (such as bond lengths or band gaps) are included that would require the knowledge of the specific perovskite structure. This enables direct evaluation of the descriptors, as is also possible for the Goldschmidt tolerance factor. The included features are the effective crystal radii of the metal, halogen, and organic cation,[89] as well as the electronegativity and polarizability of the metal and halogen atoms. The latter two features have shown to be useful in multiple studies combining HOIPs and predictive techniques.[88,90] Differently from previous studies and in order to easily encode the nature of the organic cations, here some additional bond counts were included: the number of C−H, N−H and O−H bonds as well as the number of π bonds. Hydroxylammonium is the only cation in the dataset that contains an O−H bond. There are four organic cations that contain π bonds: formamidinium, acetamidinium, guanidinium, and imidazolium with, respectively, 2, 3, 3, and 5 π bonds. Evidently, there is a correlation between the electronegativity, χ, and the polarizability, α, of the halogens and the metal; however, the SISSO algorithm does not suffer from highly correlated features.[66]

RESULTS AND DISCUSSION

Connecting Stability of HOIPs with Composition and Structure. In this section, we will assess the noncovalent binding interactions between the organic cation and the halogen atoms in a single unit cell consisting of 1 (approximate) cube formed by the metal atoms, plus the 12 halogens along the edges of the cube and the single organic cation inside the cube. As stated before, we consider the total binding strength of all cation-X interactions called E_{total} and the binding strength corresponding with the halogen that has the weakest interaction with the cation called E_{minX}. Since there are three different halogens, $E_{minX} \leq E_{total}/3$.

The distribution of all E_{total} values obtained for all 190 HOIPs is presented in Figure 1. The type of halogen atom most clearly affects E_{total}. With fluorine, E_{total} is about twice as high as for heavier halogens. This trend is not only found in HOIPs[91] but is typically for any D−H···X−M interaction where D is either C, N, or O.[92] The high electronegativity of fluorine causes the X−M bonds to be of considerably polar character leaving a strong negatively electrostatic potential around the atom and causing strong hydrogen bonds, generally called metal-assisted hydrogen bonds.[93] Changing the metal has only a minor influence, in agreement with previous studies.[94] E_{total} seems to be only slightly higher for germanium. Since the electronegativity of the metals is very similar, it is most likely attributed to the smaller covalent radius of germanium (Ge:122 pm, Sn:140 pm, and Pb:146 pm)[95] causing slightly shorter and stronger bonds.

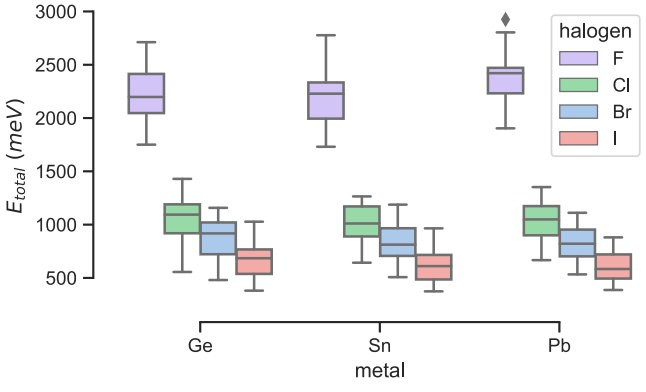

Figure 1. Box plot showing the distribution of the E_{total} values grouped by the metal and the halogen. The boxes show the quartiles of the dataset, while the whiskers are extended to 1.5 times the interquartile range.

To compare the effect of the organic cation, we look at the fractional deviations of the individual E_{minX} values with respect to the average of all E_{minX} values per halogen and metal. The fractional deviation f is defined as $f(E_{minX}) = \frac{E_{minX} - \bar{E}^{XM}_{minX}}{\bar{E}^{XM}_{minX}}$, where $\bar{E}^{XM}_{minX}$ is the average of all E_{minX} values having halogen X and metal M. The results are presented in Figure 2.

It is remarkable that methylammonium, by far the most used in HOIPs, has the lowest E_{minX} values, that is, the weakest halogen−cation bond strengths, which well explains the degradation of $MAPbI_3$ to PbI_2 under UV light even without moisture or oxygen present.[96] The observed trend can roughly be attributed to the size or the number of hydrogen atoms in the cation. Svane et al.,[64] who studied four organic cations in formate perovskites, found strong H bonds in guanidinium and hydrazinium and weak ones in dimethylammonium and azetidinium. This agrees with the trend found here, except for the hydrazinium cation that has a remarkable low E_{minX} value.

Svane et al.[64] also studied the HOIPs $MAPbX_3$ and $FAPbX_3$ with X = Cl, Br, and I. Remarkably, they found slightly lower total electrostatic energies and hydrogen bonding energies for FA than for MA. We also found slightly lower hydrogen bonding energies for FA, but our results also further suggest that the E_{total} values for FA are slightly higher than those for MA because of π···X interactions (see Supporting Information Section 1). Interestingly, FA ranks much lower for E_{total}, than for E_{minX}. This means that, despite FA having comparable total energy interaction as MA, it more evenly binds to the three different halogens, while MA leaves some halogens only weakly coupled. The relatively higher ranking in E_{minX} versus E_{total} is observed for all four cations having π bonds.

In Table 1 the five structures with the minimum and maximum E_{total} and E_{minX} are given. Since the cation−halogen bond strength decreases with decreasing electronegativity of the halogen, it is logical that all minimum structures contain iodine, while all maximum structures contain fluorine. Guanidinium is the only cation that has both a high E_{total} and a high E_{minX}. Although hydrazinium and ammonium have the lowest E_{total}, methylammonium and hydroxylammonium have the weakest coupling to a halogen atom. Hydroxylammonium has the most noticeable result since it binds very strongly to one halogen via an O−H···X − M bond while it leaves other halogens only weakly bound.

Noticeable binding characteristics are found in specific structures. We discuss at first some structures with either very small or high E_{minX}. Next, we show the structures having the highest and lowest E_{total} followed by a discussion of the structures that have the weakest and strongest individual bonds. By looking at these structures, we can analyze the very nature of the bonds that contribute to E_{minX} and the influence of the orientation of the cation.

https://doi.org/10.1021/acs.jpcc.1c07295
J. Phys. Chem. C 2021, 125, 25316−25326

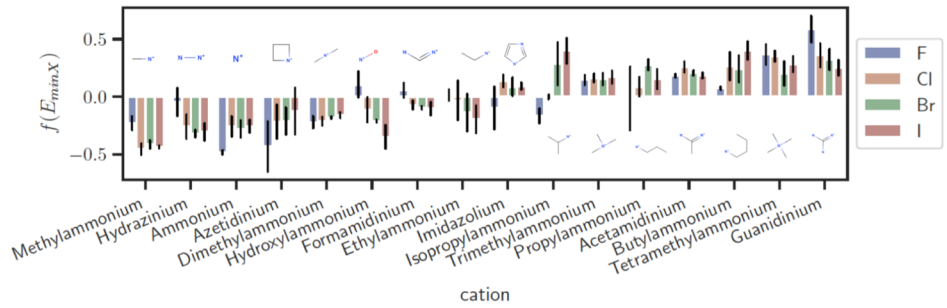

Figure 2. Bar plot showing the fractional deviations from the mean of the E_{minX} values. The boxes show the standard deviation within the three points per metal. The cations are ordered by the mean of bars for Cl, Br, and I. The cation structures are shown without their hydrogen atoms.

Table 1. Table Giving the Five Structures with the Lowest and the Five with the Highest Cation−Halogen Bond Strengths[a]

#	M	X	cation	E_{total}	#	M	X	cation	E_{minX}
1	Sn	I	hydrazinium	374	**11**	Pb	I	methylammonium	92
2	Ge	I	ammonium	380	**12**	Sn	I	methylammonium	93
3	Pb	I	hydrazinium	387	**13**	Pb	I	hydroxylammonium	95
4	Pb	I	ammonium	396	**14**	Ge	I	hydroxylammonium	103
5	Sn	I	ammonium	403	**15**	Ge	I	methylammonium	104
6	Ge	F	hydroxylammonium	2549	**16**	Ge	F	propylammonium	769
7	Ge	F	guanidinium	2712	**17**	Pb	F	tetramethylammonium	796
8	Sn	F	guanidinium	2777	**18**	Ge	F	guanidinium	815
9	Pb	F	acetamidinium	2804	**19**	Sn	F	guanidinium	879
10	Pb	F	guanidinium	2925	**20**	Pb	F	guanidinium	931

[a]Note that some structures appear in both columns: **7** = **18**, **8** = **19** and **10** = **20**. All values are in meV. The "M" and "X" columns give the type of metal and halogen, respectively.

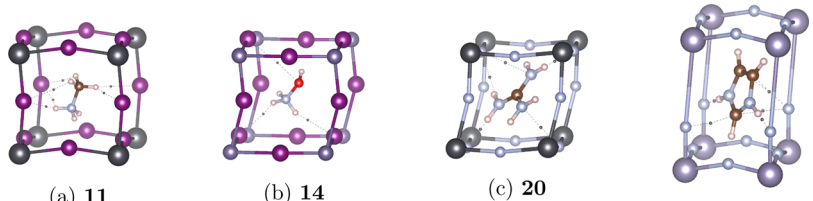

Figure 3. Four HOIP structures with the BCPs to only one type of halogen shown as little black dots, connected by dashed lines. The atoms are colored as Pb-black, I-purple, Ge-dark(steel) blue, F-blue, O-red, N-blue, C-brown, and H-white.

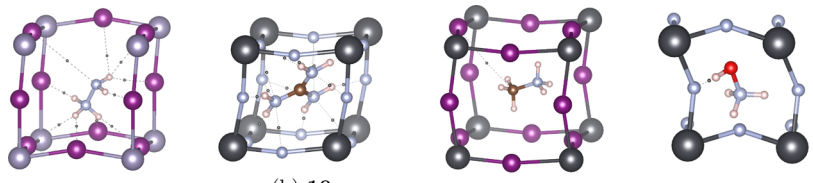

Figure 4. Four HOIP structures with the BCPs shown as little black dots connected by dashed lines. The atoms are colored as Pb-black, I-purple, Ge-dark(steel) blue, F-blue, O-red, N-blue, C-brown, and H-white.

In Figure 3 only the BCPs that contribute to E_{minX} are shown. Structure **11** (methylammonium lead iodide) has the lowest E_{minX} value of only 92 meV. The weakest bound halogens are oriented approximately in the plane perpendicular to the C−N bond. Since neither the methyl nor the amine group is oriented toward these halogens, the bond lengths are larger and the binding is weaker. In total, the C−H···I bonds account for more than 50% of E_{minX} illustrating the importance of these bonds in HOIPs (and $MAPbI_3$ in particular), as previously partially advocated by Varadwaj et al.[62,85] Another interesting structure with a very low E_{minX} of only 103 meV is **14** (hydroxylammonium germanium iodide). The weakest bound halogens in **14** are only bound with two long hydrogen bonds of 2.9 and 3.4 Å (together 86% of E_{minX}) and a long chalcogen bond of 4.2 Å (O···F).

Structure **20** (guanidinium lead fluoride) has the highest E_{minX} with two hydrogen bonds in the plane of the molecule that account together for 65% of E_{minX}, and the other 35% is caused by π−anion interactions, thus adding a significant part to E_{minX}. Additionally, the structure of imidazolium tin fluoride (**21**) is given in Figure 3 because it has the halogens with the strongest interactions to the cation. The total binding energy

https://doi.org/10.1021/acs.jpcc.1c07295
J. Phys. Chem. C 2021, 125, 25316−25326

to these halogen atoms is 1290 meV, of which the two H bonds account for 79% and the rest are π−anion interactions.

The structures with the lowest and highest E_{total}, **1** and **10** (hydrazinium tin iodide and guanidinium lead fluoride), are shown in Figure 4. **1** has 10 BCPs, while **10** has 15. It is surprising that E_{total} for hydrazinium is even lower than that for ammonium. This is most likely caused by the more favorable cation position in the ammonium structure where there are three strong nonbifurcated H bonds, while the fourth hydrogen of ammonium has a trifurcated H bond, that is, a single hydrogen participating in 3 H bonds. This orientation is possible because ammonium can align its threefold rotational axis with the ⟨111⟩ direction of the cube. In structure **10**, 65% of E_{total} is caused by the strong H bonds in the plane of the guanidinium molecule. Due to the high symmetrical arrangement, guanidinium binds very evenly to all three types of halogens, and thus $E_{minX} \lesssim 3E_{total}$. This provides a quantitative explanation of the exceptional binding properties of guanidinium in HOIPs. The combination of the strong H bonds and the bonds not being free to rotate due to π-conjugation causes guanidinium to stay strongly bound at elevated temperatures as well.[64] Additionally, note that guanidinium has a three-fold rotational axis aligned with the ⟨111⟩ direction of the cube, so it binds similarly with all three halogens.

In Figure 4 also, the structures with the weakest and strongest bond present in the dataset are depicted as **11** and **22**, respectively (methylammonium lead iodide and hydroxylammonium lead fluoride). The weakest BCP is present in $MAPbI_3$ with only 7.7 meV. This bond also corresponds with the BCP that has the lowest ρ_0 and $\nabla^2\rho$ values of 0.00128 and 0.0037, respectively. This bond can be characterized as a carbon−halogen bond C···I, a very weak so-called tetrel bond, only reported for $MAPbBr_3$ in one previous work.[85] The strongest bond in **22** is an O−H···F bond. From the whole dataset, this bond also is the shortest and has the highest density at its BCP (and second but highest density gradient). Note that this bond causes a large tilting angle in the perovskite. Large tilting angles often cause structural instability and non-photoactive phases.[91,97] Hence, to prevent large tilting angles, it is best for the cation to bind all halogens strongly but evenly.

In summary, we can conclude that having a strong cation−halogen bond does not mean having a high E_{minX} as in hydroxylammonium and that methylammonium has a low E_{minX} due to the difficulty to couple to all three halogens, while guadinium binds very effectively.

SISSO RESULTS

To increase our understanding of how the chemical composition and, in particular, the cation structure influence the binding in HOIPs, we formulate here new mathematical descriptors composed from elementary topological features that best correlate with E_{minX}. To this end, we apply the symbolic regression technique called SISSO, which designs mathematical descriptors by applying simple mathematical operators to the user-provided input values, that is, the elementary "raw" features. For the halogen and the metal, the included elementary features are their polarizability α, vdW radius r, and electronegativity χ. The structure of the cation is encoded via its effective radius and relevant bond counts: the number of C−H, N−H, O−H, and π bonds. (A table of all features for all structures can be found in the Supporting Information.) Note that to obtain these elementary features, no knowledge of the structures is required, and evaluation of the descriptors should be as straightforward as evaluating the Goldschmidt tolerance factor. The cation radii are only an approximation since most of the cations are not even close to being spherical. Nevertheless, they have been shown to be effective quantities within applications of predictive techniques on HOIPs.[87,89,98]

Since we already know that the type of halogen plays an important role, we ran SISSO in two ways: in the first case, we apply SISSO on the whole dataset, named single task. In the second case, we apply the multitask learning capability of SISSO where the dataset is split into a subset for each halogen. Next, SISSO tries to find global descriptors, while for each set, different coefficients are optimized. So, for a multiset multidimensional SISSO run, E_{minX} for a given HOIP $\mathcal{X}$ is $E_{minX}(\mathcal{X}) = c_i^0 + \sum_{j=1}^{N_{dim}} c_i^j d^j(\mathcal{X})$ where c_i^0 is an intercept of the ith task, c_i^j is the coefficient of the ith task of the jth dimension, and d^j is the descriptor of the jth dimension, thus being identical among all tasks.

To allow for scientific interpretability, we apply a maximum to the descriptor complexity. This cutoff is effectively a hyperparameter to be chosen freely by the user. In Figure 5 the errors as a function of dimension and complexity cutoff are shown for single and multitask SISSO. Multitask SISSO always outperforms single-task SISSO, which is expected since it has to account for less variance within the subsets, and there are 4 times more fitted coefficients. Changing the complexity cutoff in multitask SISSO from 2 to 3 does not give any significant improvement.

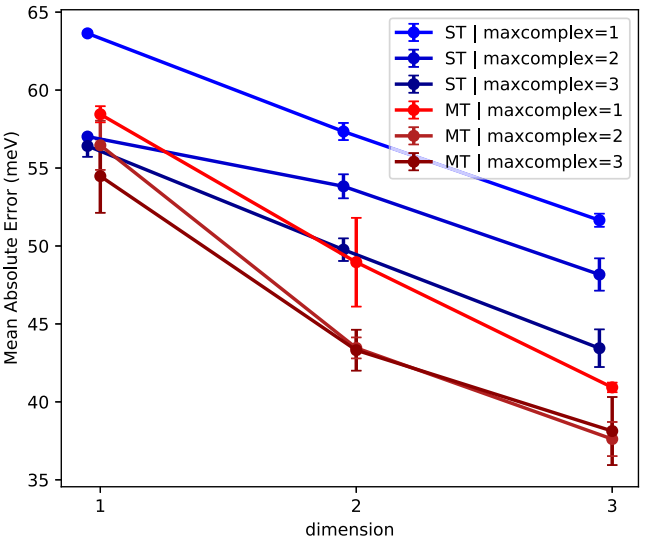

Figure 5. SISSO MAEs versus dimension and maxcomplexity. ST = single task; MT = multitask. For each setting, SISSO is run five times via cross-validation with test sets of 20% of the data. The error bars indicate the minimum and maximum MAEs of the five runs, and the central dot is placed at the average MAE.

The SISSO descriptors of single and multitask corresponding to the lines in Figure 5 with maxcomplexity 2 are shown in Table 2. In the single-task results, the halogen features are always present, accounting for the large difference in E_{minX} for the different halogens. In the multitask results, the effect of the halogens is already taken into account via splitting the total dataset into four smaller sets, so the descriptors consider more

https://doi.org/10.1021/acs.jpcc.1c07295
J. Phys. Chem. C 2021, 125, 25316−25326

Table 2. Table Showing the Descriptors as Found by SISSO Setting the Maximum Complexity at 2[a]

dim	task	descriptors		
1D	ST	r_{cation}/r_X^2		
	MT	$N_\pi + \lvert N_{CH} - N_{NH}\rvert$		
2D	ST	r_{cation}/r_X^2	$\frac{N_{NH}*N_\pi}{\alpha_X}$	
	MT	$N_{CH} + N_{OH} + N_\pi$	$(N_{NH} + N_{OH})^2$	
3D	ST	$\frac{N_{OH} + N_\pi}{r_X}$	$\frac{N_{NH} + N_{OH}}{\alpha_X}$	$\frac{N_{CH}^2}{r_X^2}$
	MT	$N_{CH} + N_{OH} + N_\pi$,	$N_{NH} + 2N_{OH}$	$N_{CH}*\lvert N_{NH} - N_\pi\rvert$

[a]ST = single task, MT = multitask. The descriptor coefficients are not shown but given in Supporting Information Section 3.

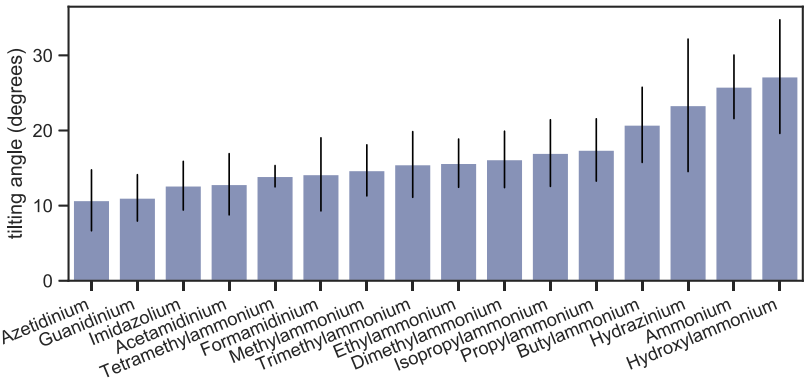

Figure 6. Average tilting angles per cation. Error bars indicate the standard deviation.

the effect of the organic cation. The results show that it is not only N_{NH} that is important but also the other bond counts N_{CH}, N_{OH}, and N_π. The cation radius appears in the low-dimension results but disappears in the 3D result. This illustrates that the radius of the cation is not important per se, but only inasmuch the radius of the cation correlates with the number of bonding partners of the cation. The features accounting for the metal atom do not appear at all, indicating that the metal has no significant influence on E_{minX}. It is remarkable that N_π plays a dominant role in the SISSO descriptors for E_{minX} as it is included in the multitask 1D descriptor. These results further illustrate the importance of weak interactions for E_{minX}.

In the 3D multitask descriptor, a factor 2 appears. This can occur when SISSO uses the "+" operator twice with the same feature. Here, $N_{NH} + N_{OH} + N_{OH}$ simply reduces to $N_{NH} + 2N_{OH}$. It is a generally occurring phenomenon that SISSO descriptors are found that try to balance the importance of two elementary features by constructing "weights," and $N_{NH} + 2N_{OH}$ includes elementary features N_{NH} and N_{OH} with weights 1 and 2, respectively. In this case, it is a logical consequence of the O−H···X bonds being stronger than the N−H···X bonds.

Still a significant part of the variance in E_{minX} stays unexplained by the SISSO results, showing that factors other than those of the included topological features play a role. This is not a surprise since the input features do not take into account the crystal packing. The packing factor is important since some cations can orient themselves more optimally than others to form strong noncovalent interactions to each halogen. As an example, the smallest cation, ammonium, can form a strong interaction with each of the tree types of halogens, explaining why its E_{minX} is higher than those of methylammonium and hydrazinium. Nevertheless [given that the baseline mean absolute error (MAE) is 130 meV], it is remarkable that around 70% of the variance can be explained using only these basic features, providing already a great understanding in the factors determining E_{minX}.

Last, we compare our results for the prediction of halide perovskite stability with the Goldschmidt tolerance factor, commonly used to predict if a material will be stable in the perovskite conformation and given by[98]

$$t = \frac{r_{cation} + r_X}{\sqrt{2}\,(r_M + r_X)} \tag{2}$$

Although improved stability factors have been designed,[99] the general trend still applies that for a perovskite structure to be stable, t has to be approximately between 0.85 and 1.12.[100,101] Our results show that roughly E_{minX} and E_{total} increase with larger cations, while the Goldschmidt factor puts a limit at how large these cations can be, and a balanced solution has to be chosen. Hence, although our results show that HOIPs will become more structurally stable w.r.t. halogen migration when the cation binds more strongly to the halogens, the perovskite structure itself might become unstable when larger cations are used. For example, guanidinium germanium iodide has $t = 1.2$, thus lying outside the stability window, while guanidinium lead iodide, having a larger metal, is stable ($t = 1.03$). Nevertheless, also small additions of other cations might improve the perovskite stability while keeping the Goldschmidt factor within the acceptable range. When t is too high, the tilting angles of the MX_6 octahedrons increase leading to non-photoactive phases. For example, at room temperature, $FAPbI_3$ exists in a non-photoactive phase, while when FA is mixed with MA or Cs, the photoactive phase becomes stable.[74,100]

For what concerns the most common cations (MA and FA), our results generalize a previous study[35] where only the MA

https://doi.org/10.1021/acs.jpcc.1c07295
J. Phys. Chem. C 2021, 125, 25316−25326

and FA cations were compared, showing higher binding strengths for the FA cation. Indeed, our findings generalize the higher E_{total} of FA than MA to any type of halogen or metal, but by looking at E_{minX} instead of only looking at E_{total}, our work makes an even stronger case to use FA instead of MA since MA binds some halogens particularly weakly.

In Figure 6 the average tilting angles are given for each organic cation. The extent of octahedral tilting is a complex phenomenon that is driven by the interplay between many interactions.[62] Bernasconi et al.[102] found that the tilting angle in $MAPbX_3$ (with X is Cl, Br, and I) correlates with the strongest hydrogen bond. As one can see from structure **11** in $MAPbI_3$, the tilting is oriented toward the ammonium group. This trend is also more generally observed as the tilting angle is the largest for hydroxylammonium since it forms a very strong hydrogen bond (see structure **23**). Yet, the trend is more intricate since the cation with the second highest tilting is ammonium. The large tilting observed for ammonium can be attributed to the small size of the cation and also to the strong hydrogen bonding of ammonium to three halogens, pulling these halogens closer. Additionally, large tilting angles are observed for structures with an ammonium group and an additional alkane group (methyl-, ethyl-, propyl-, isopropyl-, tetrabutyl-, and dimethylammonium) and for all structures where the stronger hydrogen bonds of N−H groups on one side of the cavity create a pronounced tilting effect. The smallest tilting angles are observed for HOIPs with the azetinidinium cation. Here, the two N−H groups only bind to one type of halogen, while the other two types of halogens are binding exactly evenly by all C−H groups, thus giving an almost zero tilting angle for two dimensions and only a slight tilting in the dimension where the two N−H groups bind with the halogens. Small tilting angles are also observed for guanidinium since it binds very evenly to all 12 halogens of the cavity.

Our results show that there is a meaningful relation between the bond counts of the cation and the HOIP stability. While former machine learning models are only based on effective radii and electronegativity values,[87,103,104] from our results, it can be induced that inclusion of the bond counts, especially when combined like in the SISSO descriptors, expresses useful quantities. For organic cations, these bond counts give far more information than only the effective radii since the presence of π bonds or O−H bonds is crucial information not captured in only an effective radius. Specific bond counts affect the noncovalent interactions, which dictate tilting angles, that then have an influence on carrier mobility and band gaps.

CONCLUSIONS

HOIPs represent a potential game-changer technology to harvest solar energy. Still, the intrinsic instability and degradation due to external factors of such systems prevent large-scale production. The present study has identified the key aspects that contribute to the stabilization of halide ions in HOIPs, the major species that undergoes migration in the absence and under the effect of different external factors, creating instability and degradation.

Our work has revealed the fundamental bond and composition properties that most affect the halogen−cation interactions in hybrid perovskites in a large chemical space. This allows us to give a rationale of previous results, based on smaller spaces, and to highlight previous misconceptions and overlooked aspects. In particular, we unveil the reasons of an improved stability given by the halogen F, the origin of the higher stability offered by FA compared to MA, which shows to be different from previous explanations in the literature, and the reason behind the exceptional case of overall stronger bonds for guanidinium. A clear inverse power law between bond lengths and density at the BCPs is also found. Our results highlight the importance of the cation-halide interactions and the urge to differentiate between different halide positions. We have corroborated in a quantitative and first-principles manner the importance of noncovalent interactions other than N−H···I, such as C−H···I and N/C···I for $MAPbI_3$, advocated in a previous work,[62] confirming that the neglect of such interactions in the majority of studies may lead to potentially wrong criteria for the design of new HOIPs. We did this not only for MA but for a whole array of 16 different organic cations. Additionally, in some cations such as FA, also π···X are found. We show that these weak interactions have a significant role to bind the halogen atoms and thus are expected to be important to prevent halogen migration. Therefore, the in-depth understanding of weak noncovalent interactions is fundamental in the molecular design of new, more stable HOIPs. Moreover, as the most prevalent cation, MA even has the lowest E_{minX}, and there is ample room for cation substitution to increase the cation−halogen coupling.

We found new mathematical, physically meaningful descriptors that identify the factors that dominate the coupling between the halogens and cations. We showed that the factors in order of importance are the type of halogen, the presence of π···X bonding, and the number of hydrogen bond donors including C−H. Bonds other than H bonds have been overlooked in previous studies, like the considerable importance of π bonds in binding to the weakest halogen bonds. We show that bond counts are more meaningful than only the effective radii as used in the prevalent Goldschmidt tolerance factor. Moreover, the found descriptors unveil the importance of π-interactions for strong cation-halide interactions. Based on this work, we suggest HOIP stabilization by inclusion of larger cations, preferably those having π bonds. Guanidinium proves to be the most effective cation due to multiple N−H hydrogen bond donors, a large π-conjugated system, and its efficient packing due to alignment with the ⟨111⟩ direction, thus binding evenly with all halogens.

Our work focuses on enhanced stability via a robust design approach for strengthening molecular bonds and offers an alternative route to the different approaches previously used for HOIPs. We believe that our work will motivate the investigation of new hybrid perovskite materials with strong and balanced noncovalent interactions. The new descriptors can be used to train machine learning algorithms for even larger chemical spaces and to drive the design of HOIPs with chemical bonding enhancement and immobilization of the potentially migrating ions. As our study focuses on shaping atomic-scale properties within one unit cell, it potentially offers the possibility to design large-size single crystals that do not segregate and do not form grains.

ASSOCIATED CONTENT

Supporting Information

The Supporting Information is available free of charge at https://pubs.acs.org/doi/10.1021/acs.jpcc.1c07295.

SISSO input file listing all input features (TXT)

https://doi.org/10.1021/acs.jpcc.1c07295
J. Phys. Chem. C 2021, 125, 25316−25326

A comma-separated file listing all 548 HOIPs adhering to a perovskite structure with their continuous symmetry measures for cubicity, E_{total}, E_{minX}, and $E_{atomozation}$ values (TXT)

Plot of fractional mean deviations from E_{total} instead of E_{minX}; box plot and bar plot for the total set of 548 perovskite-structured HOIPs in the dataset; SISSO intercepts and coefficients; and correlations between bond lengths and BCPs (PDF)

AUTHOR INFORMATION

Corresponding Author

Johannes L. Teunissen − *Royal Belgian Institute for Space Aeronomy, 1180 Brussels, Belgium; Université Lille, CNRS UMR 8520—IEMN—Institute of Electronics, Microelectronics and Nanotechnology, F-59000 Lille, France;* orcid.org/0000-0002-0188-6064; Email: jlteunissen@gmail.com

Author

Fabiana Da Pieve − *Royal Belgian Institute for Space Aeronomy, 1180 Brussels, Belgium;* orcid.org/0000-0001-6985-9145

Complete contact information is available at: https://pubs.acs.org/10.1021/acs.jpcc.1c07295

Notes

The authors declare no competing financial interest.

ACKNOWLEDGMENTS

This work has received funding from the Research Executive Agency under the EU's Horizon 2020 Research and Innovation program ESC2RAD (grant ID 776410). We are grateful to PRACE for granting us access to the computational resources of the Joliot-Curie SKL at CEA (France) (PRACE Project: 2019215186), and we thank the Space POLE HPC for providing the resources for the SISSO calculations.

REFERENCES

(1) Jeon, N. J.; Noh, J. H.; Yang, W. S.; Kim, Y. C.; Ryu, S.; Seo, J.; Seok, S. I. Compositional Engineering of Perovskite Materials for High-Performance Solar Cells. *Nature* **2015**, *517*, 476−480.

(2) Brown, C. R.; Eperon, G. E.; Whiteside, V. R.; Sellers, I. R. Potential of High-Stability Perovskite Solar Cells for Low-Intensity-Low-Temperature (LILT) Outer Planetary Space Missions. *ACS Appl. Energy Mater.* **2019**, *2*, 814−821.

(3) Cardinaletti, I.; Vangerven, T.; Nagels, S.; Cornelissen, R.; Schreurs, D.; Hruby, J.; Vodnik, J.; Devisscher, D.; Kesters, J.; D'Haen, J.; et al. Organic and Perovskite Solar Cells for Space Applications. *Sol. Energy Mater. Sol. Cells* **2018**, *182*, 121−127.

(4) Yang, J.; Bao, Q.; Shen, L.; Ding, L. Potential Applications for Perovskite Solar Cells in Space. *Nano Energy* **2020**, *76*, 105019.

(5) Best Research-Cell Efficiency Chart. www.nrel.gov/pv/cell-efficiency.html, 2021; (accessed: January, 2021).

(6) Green, M. A.; Hishikawa, Y.; Warta, W.; Dunlop, E. D.; Levi, D. H.; Hohl-Ebinger, J.; Ho-Baillie, A. W. H. Solar Cell Efficiency Tables (Version 50). *Prog. Photovoltaics* **2017**, *25*, 668−676.

(7) Snaith, H. J. Perovskites: The Emergence of a New Era for Low-Cost, High-Efficiency Solar Cells. *J. Phys. Chem. Lett.* **2013**, *4*, 3623−3630.

(8) Kaltenbrunner, M.; Adam, G.; Głowacki, E. D.; Drack, M.; Schwödiauer, R.; Leonat, L.; Apaydin, D. H.; Groiss, H.; Scharber, M. C.; White, M. S.; et al. Flexible high power-per-weight perovskite solar cells with chromium oxide-metal contacts for improved stability in air. *Nat. Mater.* **2015**, *14*, 1032−1039.

(9) Burschka, J.; Pellet, N.; Moon, S.-J.; Humphry-Baker, R.; Gao, P.; Nazeeruddin, M. K.; Grätzel, M. Sequential Deposition as a Route to High-Performance Perovskite-Sensitized Solar Cells. *Nature* **2013**, *499*, 316−319.

(10) Lang, F.; Nickel, N. H.; Bundesmann, J.; Seidel, S.; Denker, A.; Albrecht, S.; Brus, V. V.; Rappich, J.; Rech, B.; Landi, G.; et al. Radiation Hardness and Self-Healing of Perovskite Solar Cells. *Adv. Mater.* **2016**, *28*, 8726−8731.

(11) Miyazawa, Y.; Ikegami, M.; Miyasaka, T.; Ohshima, T.; Imaizumi, M.; Hirose, K. *Evaluation of Radiation Tolerance of Perovskite Solar Cell for Use in Space 2015 IEEE 42nd Photovoltaic Specialist Conference (PVSC)*; IEEE, 2015; pp 1−4.

(12) Miyazawa, Y.; Ikegami, M.; Chen, H.-W.; Ohshima, T.; Imaizumi, M.; Hirose, K.; Miyasaka, T. Tolerance of Perovskite Solar Cell to High-Energy Particle Irradiations in Space Environment. *iScience* **2018**, *2*, 148−155.

(13) Huang, J.; Kelzenberg, M. D.; Espinet-González, P.; Mann, C.; Walker, D.; Naqavi, A.; Vaidya, N.; Warmann, E.; Atwater, H. A. *Effects of Electron and Proton Radiation on Perovskite Solar Cells for Space Solar Power Application. 2017 IEEE 44th Photovoltaic Specialist Conference (PVSC)*; IEEE, 2017, pp 1248−1252.

(14) Kojima, A.; Teshima, K.; Shirai, Y.; Miyasaka, T. Organometal Halide Perovskites as Visible-Light Sensitizers for Photovoltaic Cells. *J. Am. Chem. Soc.* **2009**, *131*, 6050−6051.

(15) Yue, L.; Yan, B.; Attridge, M.; Wang, Z. Light Absorption in Perovskite Solar Cell: Fundamentals and Plasmonic Enhancement of Infrared Band Absorption. *Sol. Energy* **2016**, *124*, 143−152.

(16) De Wolf, S.; Holovsky, J.; Moon, S.-J.; Löper, P.; Niesen, B.; Ledinsky, M.; Haug, F.-J.; Yum, J.-H.; Ballif, C. Organometallic Halide Perovskites: Sharp Optical Absorption Edge and Its Relation to Photovoltaic Performance. *J. Phys. Chem. Lett.* **2014**, *5*, 1035−1039.

(17) McMeekin, D. P.; Sadoughi, G.; Rehman, W.; Eperon, G. E.; Saliba, M.; Hörantner, M. T.; Haghighirad, A.; Sakai, N.; Korte, L.; Rech, B.; et al. A Mixed-Cation Lead Mixed-Halide Perovskite Absorber for Tandem Solar Cells. *Science* **2016**, *351*, 151−155.

(18) Saba, M.; Quochi, F.; Mura, A.; Bongiovanni, G. Excited State Properties of Hybrid Perovskites. *Acc. Chem. Res.* **2016**, *49*, 166−173.

(19) Motta, C.; El-Mellouhi, F.; Sanvito, S. Charge Carrier Mobility in Hybrid Halide Perovskites. *Sci. Rep.* **2015**, *5*, 12746.

(20) Wehrenfennig, C.; Eperon, G. E.; Johnston, M. B.; Snaith, H. J.; Herz, L. M. High Charge Carrier Mobilities and Lifetimes in Organolead Trihalide Perovskites. *Adv. Mater.* **2014**, *26*, 1584−1589.

(21) Zheng, F.; Wang, L.-w. Large Polaron Formation and Its Effect on Electron Transport in Hybrid Perovskites. *Energy Environ. Sci.* **2019**, *12*, 1219−1230.

(22) Frost, J. M.; Whalley, L. D.; Walsh, A. Slow Cooling of Hot Polarons in Halide Perovskite Solar Cells. *ACS Energy Lett.* **2017**, *2*, 2647−2652.

(23) Ambrosio, F.; Wiktor, J.; De Angelis, F.; Pasquarello, A. Origin of low electron-hole recombination rate in metal halide perovskites. *Energy Environ. Sci.* **2018**, *11*, 101−105.

(24) Schlipf, M.; Poncé, S.; Giustino, F. Carrier Lifetimes and Polaronic Mass Enhancement in the Hybrid Halide Perovskite $CH_3NH_3PbI_3$ from Multiphonon Fröhlich Coupling. *Phys. Rev. Lett.* **2018**, *121*, 086402.

(25) Miyata, A.; Mitioglu, A.; Plochocka, P.; Portugall, O.; Wang, J. T.-W.; Stranks, S. D.; Snaith, H. J.; Nicholas, R. J. Direct measurement of the exciton binding energy and effective masses for charge carriers in organic-inorganic tri-halide perovskites. *Nat. Physics* **2015**, *11*, 582−587.

(26) Srimath Kandada, A. R.; Petrozza, A. Photophysics of Hybrid Lead Halide Perovskites: The Role of Microstructure. *Acc. Chem. Res.* **2016**, *49*, 536−544.

(27) Ponseca, C. S.; Savenije, T. J.; Abdellah, M.; Zheng, K.; Yartsev, A.; Pascher, T.; Harlang, T.; Chabera, P.; Pullerits, T.; Stepanov, A.; et al. Organometal Halide Perovskite Solar Cell Materials Rationalized: Ultrafast Charge Generation, High and Microsecond-Long Balanced Mobilities, and Slow Recombination. *J. Am. Chem. Soc.* **2014**, *136*, 5189−5192.

(28) Stranks, S. D.; Eperon, G. E.; Grancini, G.; Menelaou, C.; Alcocer, M. J. P.; Leijtens, T.; Herz, L. M.; Petrozza, A.; Snaith, H. J. Electron-Hole Diffusion Lengths Exceeding 1 Micrometer in an Organometal Trihalide Perovskite Absorber. *Science* **2013**, *342*, 341−344.
(29) Boyd, C. C.; Cheacharoen, R.; Leijtens, T.; McGehee, M. D. Understanding Degradation Mechanisms and Improving Stability of Perovskite Photovoltaics. *Chem. Rev.* **2019**, *119*, 3418−3451.
(30) Berry, J.; Buonassisi, T.; Egger, D. A.; Hodes, G.; Kronik, L.; Loo, Y.-L.; Lubomirsky, I.; Marder, S. R.; Mastai, Y.; Miller, J. S.; et al. Hybrid Organic-Inorganic Perovskites (HOIPs): Opportunities and Challenges. *Adv. Mater.* **2015**, *27*, 5102−5112.
(31) Zhang, Y.-Y.; Chen, S.; Xu, P.; Xiang, H.; Gong, X.-G.; Walsh, A.; Wei, S.-H. Intrinsic Instability of the Hybrid Halide Perovskite Semiconductor $CH_3NH_3PbI_3$. *Chin. Phys. Lett.* **2018**, *35*, 036104.
(32) Akbulatov, A. F.; Frolova, L. A.; Dremova, N. N.; Zhidkov, I.; Martynenko, V. M.; Tsarev, S. A.; Luchkin, S. Y.; Kurmaev, E. Z.; Aldoshin, S. M.; Stevenson, K. J.; et al. Light or Heat: What Is Killing Lead Halide Perovskites under Solar Cell Operation Conditions? *J. Phys. Chem. Lett.* **2020**, *11*, 333−339.
(33) Eames, C.; Frost, J. M.; Barnes, P. R. F.; O'Regan, B. C.; Walsh, A.; Islam, M. S. Ionic Transport in Hybrid Lead Iodide Perovskite Solar Cells. *Nat. Commun.* **2015**, *6*, 7497.
(34) Meggiolaro, D.; Motti, S. G.; Mosconi, E.; Barker, A. J.; Ball, J.; Andrea Riccardo Perini, C.; Deschler, F.; Petrozza, A.; De Angelis, F. Iodine Chemistry Determines the Defect Tolerance of Lead-Halide Perovskites. *Energy Environ. Sci.* **2018**, *11*, 702−713.
(35) Oranskaia, A.; Schwingenschlögl, U. Suppressing X-Migrations and Enhancing the Phase Stability of Cubic $FAPbX_3$ (X = Br, I). *Adv. Energy Mater.* **2019**, *9*, 1901411.
(36) Futscher, M. H.; Lee, J. M.; McGovern, L.; Muscarella, L. A.; Wang, T.; Haider, M. I.; Fakharuddin, A.; Schmidt-Mende, L.; Ehrler, B. Quantification of Ion Migration in $CH_3NH_3PbI_3$ Perovskite Solar Cells by Transient Capacitance Measurements. *Mater. Horiz.* **2019**, *6*, 1497−1503.
(37) Khan, R.; Ighodalo, K. O.; Xiao, Z. *Soft-Matter Thin Film Solar Cells*; AIP Publishing: Melville, New York, 2020. Chapter 3.
(38) Adinolfi, V.; Yuan, M.; Comin, R.; Thibau, E. S.; Shi, D.; Saidaminov, M. I.; Kanjanaboos, P.; Kopilovic, D.; Hoogland, S.; Lu, Z.-H.; et al. The In-Gap Electronic State Spectrum of Methylammonium Lead Iodide Single-Crystal Perovskites. *Adv. Mater.* **2016**, *28*, 3406−3410.
(39) Yin, W.-J.; Shi, T.; Yan, Y. Unique Properties of Halide Perovskites as Possible Origins of the Superior Solar Cell Performance. *Adv. Mater.* **2014**, *26*, 4653−4658.
(40) Du, M.-H. Density Functional Calculations of Native Defects in $CH_3NH_3PbI_3$: Effects of Spin−Orbit Coupling and Self-Interaction Error. *J. Phys. Chem. Lett.* **2015**, *6*, 1461−1466.
(41) Meggiolaro, D.; De Angelis, F. First-Principles Modeling of Defects in Lead Halide Perovskites: Best Practices and Open Issues. *ACS Energy Lett.* **2018**, *3*, 2206−2222.
(42) Wolf, M. J.; Ghosh, D.; Kullgren, J.; Pazoki, M. Characterizing MAPbI3 with the aid of first principles calculations. In *Micro and Nano Technologies*; Pazoki, M., Hagfeldt, A., Edvinsson, T., Eds.; Elsevier, 2020; pp 217−236.
(43) Tong, C.-J.; Li, L.; Liu, L.-M.; Prezhdo, O. V. Synergy between Ion Migration and Charge Carrier Recombination in Metal-Halide Perovskites. *J. Am. Chem. Soc.* **2020**, *142*, 3060−3068.
(44) Lang, F.; Shargaieva, O.; Brus, V. V.; Neitzert, H. C.; Rappich, J.; Nickel, N. H. Influence of Radiation on the Properties and the Stability of Hybrid Perovskites. *Adv. Mater.* **2018**, *30*, 1702905.
(45) Yang, M.; Zhang, T.; Schulz, P.; Li, Z.; Li, G.; Kim, D. H.; Guo, N.; Berry, J. J.; Zhu, K.; Zhao, Y. Facile Fabrication of Large-Grain $CH_3NH_3PbI_{3-x}Br_x$ Films for High-Efficiency Solar Cells *via* CH_3NH_3Br-Selective Ostwald Ripening. *Nat. Commun.* **2016**, *7*, 12305.
(46) Yi, C.; Luo, J.; Meloni, S.; Boziki, A.; Ashari-Astani, N.; Grätzel, C.; Zakeeruddin, S. M.; Röthlisberger, U.; Grätzel, M. Entropic Stabilization of Mixed A-Cation ABX_3 Metal Halide Perovskites for High Performance Perovskite Solar Cells. *Energy Environ. Sci.* **2016**, *9*, 656−662.
(47) Ferdani, D. W.; Pering, S. R.; Ghosh, D.; Kubiak, P.; Walker, A. B.; Lewis, S. E.; Johnson, A. L.; Baker, P. J.; Islam, M. S.; Cameron, P. J. Partial Cation Substitution Reduces Iodide Ion Transport in Lead Iodide Perovskite Solar Cells. *Energy Environ. Sci.* **2019**, *12*, 2264−2272.
(48) Wang, F.; Geng, W.; Zhou, Y.; Fang, H.-H.; Tong, C.-J.; Loi, M. A.; Liu, L.-M.; Zhao, N. Phenylalkylamine Passivation of Organolead Halide Perovskites Enabling High-Efficiency and Air-Stable Photovoltaic Cells. *Adv. Mater.* **2016**, *28*, 9986−9992.
(49) De Marco, N.; Zhou, H.; Chen, Q.; Sun, P.; Liu, Z.; Meng, L.; Yao, E.-P.; Liu, Y.; Schiffer, A.; Yang, Y. Guanidinium: A Route to Enhanced Carrier Lifetime and Open-Circuit Voltage in Hybrid Perovskite Solar Cells. *Nano Lett.* **2016**, *16*, 1009−1016.
(50) Yang, W. S.; Park, B.-W.; Jung, E. H.; Jeon, N. J.; Kim, Y. C.; Lee, D. U.; Shin, S. S.; Seo, J.; Kim, E. K.; Noh, J. H.; et al. Iodide management in formamidinium-lead-halide-based perovskite layers for efficient solar cells. *Science* **2017**, *356*, 1376−1379.
(51) Noh, J. H.; Im, S. H.; Heo, J. H.; Mandal, T. N.; Seok, S. I. Chemical Management for Colorful, Efficient, and Stable Inorganic-Organic Hybrid Nanostructured Solar Cells. *Nano Lett.* **2013**, *13*, 1764−1769.
(52) Saliba, M.; Matsui, T.; Seo, J.-Y.; Domanski, K.; Correa-Baena, J.-P.; Nazeeruddin, M. K.; Zakeeruddin, S. M.; Tress, W.; Abate, A.; Hagfeldt, A.; et al. Cesium-Containing Triple Cation Perovskite Solar Cells: Improved Stability, Reproducibility and High Efficiency. *Energy Environ. Sci.* **2016**, *9*, 1989−1997.
(53) Saidaminov, M. I.; Kim, J.; Jain, A.; Quintero-Bermudez, R.; Tan, H.; Long, G.; Tan, F.; Johnston, A.; Zhao, Y.; Voznyy, O.; et al. Suppression of Atomic Vacancies *via* Incorporation of Isovalent Small Ions to Increase the Stability of Halide Perovskite Solar Cells in Ambient Air. *Nat. Energy* **2018**, *3*, 648−654.
(54) Zheng, X.; Chen, B.; Dai, J.; Fang, Y.; Bai, Y.; Lin, Y.; Wei, H.; Zeng, X. C.; Huang, J. Defect Passivation in Hybrid Perovskite Solar Cells Using Quaternary Ammonium Halide Anions And Cations. *Nat. Energy* **2017**, *2*, 17102.
(55) Li, F.; Liu, M. Recent Efficient Strategies for Improving the Moisture Stability of Perovskite Solar Cells. *J. Mater. Chem. A* **2017**, *5*, 15447−15459.
(56) Li, N.; Tao, S.; Chen, Y.; Niu, X.; Onwudinanti, C. K.; Hu, C.; Qiu, Z.; Xu, Z.; Zheng, G.; Wang, L.; et al. Cation and Anion Immobilization through Chemical Bonding Enhancement with Fluorides for Stable Halide Perovskite Solar Cells. *Nat. Energy* **2019**, *4*, 408−415.
(57) Holekevi Chandrappa, M. L.; Zhu, Z.; Fenning, D. P.; Ong, S. P. Correlated Octahedral Rotation and Organic Cation Reorientation Assist Halide Ion Migration in Lead Halide Perovskites. *Chem. Mater.* **2021**, *33*, 4672−4678.
(58) Zhang, T.; Meng, X.; Bai, Y.; Xiao, S.; Hu, C.; Yang, Y.; Chen, H.; Yang, S. Profiling the Organic Cation-Dependent Degradation of Organolead Halide Perovskite Solar Cells. *J. Mater. Chem. A* **2017**, *5*, 1103−1111.
(59) Oranskaia, A.; Yin, J.; Bakr, O. M.; Brédas, J.-L.; Mohammed, O. F. Halogen Migration in Hybrid Perovskites: The Organic Cation Matters. *J. Phys. Chem. Lett.* **2018**, *9*, 5474−5480.
(60) Schottel, B. L.; Chifotides, H. T.; Dunbar, K. R. Anion-π interactions. *Chem. Soc. Rev.* **2008**, *37*, 68−83.
(61) Lee, J.-H.; Bristowe, N. C.; Bristowe, P. D.; Cheetham, A. K. Role of Hydrogen-Bonding and Its Interplay with Octahedral Tilting in $CH_3NH_3PbI_3$. *Chem. Commun.* **2015**, *51*, 6434−6437.
(62) Varadwaj, P. R.; Varadwaj, A.; Marques, H. M.; Yamashita, K. Significance of Hydrogen Bonding and Other Noncovalent Interactions in Determining Octahedral Tilting in the $CH_3NH_3PbI_3$ Hybrid Organic-Inorganic Halide Perovskite Solar Cell Semiconductor. *Sci. Rep.* **2019**, *9*, 50.
(63) Lee, J. H.; Lee, J.-H.; Kong, E.-H.; Jang, H. M. The nature of hydrogen-bonding interaction in the prototypic hybrid halide perovskite, tetragonal CH3NH3PbI3. *Sci. Rep.* **2016**, *6*, 21687.

(64) Svane, K. L.; Forse, A. C.; Grey, C. P.; Kieslich, G.; Cheetham, A. K.; Walsh, A.; Butler, K. T. How Strong Is the Hydrogen Bond in Hybrid Perovskites? *J. Phys. Chem. Lett.* **2017**, *8*, 6154−6159.
(65) Bader, R.; Bader, R. *Atoms in Molecules: A Quantum Theory; International Series of Monographs on Chemistry*; Clarendon Press, 1990.
(66) Ouyang, R.; Curtarolo, S.; Ahmetcik, E.; Scheffler, M.; Ghiringhelli, L. M. SISSO: A Compressed-Sensing Method for Identifying the Best Low-Dimensional Descriptor in an Immensity of Offered Candidates. *Phys. Rev. Mater.* **2018**, *2*, 083802.
(67) Mata, I.; Alkorta, I.; Espinosa, E.; Molins, E. Relationships between Interaction Energy, Intermolecular Distance and Electron Density Properties in Hydrogen Bonded Complexes under External Electric Fields. *Chem. Phys. Lett.* **2011**, *507*, 185−189.
(68) Abramov, Y. A. On the Possibility of Kinetic Energy Density Evaluation from the Experimental Electron-Density Distribution. *Acta Crystallogr., Sect. A: Found. Crystallogr.* **1997**, *53*, 264−272.
(69) Kumar, P. S. V.; Raghavendra, V.; Subramanian, V. Bader's Theory of Atoms in Molecules (AIM) and its Applications to Chemical Bonding. *J. Chem. Sci.* **2016**, *128*, 1527−1536.
(70) Bankiewicz, B.; Matczak, P.; Palusiak, M. Electron Density Characteristics in Bond Critical Point (QTAIM) Versus Interaction Energy Components (SAPT): The Case of Charge-Assisted Hydrogen Bonding. *J. Phys. Chem. A* **2012**, *116*, 452−459.
(71) Shahbazian, S. Why Bond Critical Points Are Not "Bond" Critical Points. *Chem.—Eur. J.* **2018**, *24*, 5401−5405.
(72) Lane, J. R.; Contreras-García, J.; Piquemal, J.-P.; Miller, B. J.; Kjaergaard, H. G. Are Bond Critical Points Really Critical for Hydrogen Bonding? *J. Chem. Theory Comput.* **2013**, *9*, 3263−3266.
(73) Kim, C.; Huan, T. D.; Krishnan, S.; Ramprasad, R. A Hybrid Organic-Inorganic Perovskite Dataset. *Sci. Data* **2017**, *4*, 170057.
(74) Ava, T. T.; Al Mamun, A.; Marsillac, S.; Namkoong, G. A Review: Thermal Stability of Methylammonium Lead Halide Based Perovskite Solar Cells. *Appl. Sci.* **2019**, *9*, 188.
(75) Goedecker, S. Minima Hopping: An Efficient Search Method for the Global Minimum of the Potential Energy Surface of Complex Molecular Systems. *J. Chem. Phys.* **2004**, *120*, 9911−9917.
(76) Lee, K.; Murray, E. D.; Kong, L.; Lundqvist, B. I.; Langreth, D. C. Higher-Accuracy Van Der Waals Density Functional. *Phys. Rev. B: Condens. Matter Mater. Phys.* **2010**, *82*, 081101.
(77) Kresse, G.; Furthmüller, J. Efficient iterative schemes forab initiototal-energy calculations using a plane-wave basis set. *Phys. Rev. B: Condens. Matter Mater. Phys.* **1996**, *54*, 11169−11186.
(78) Draxl, C.; Scheffler, M. NOMAD: The FAIR Concept for Big Data-Driven Materials Science. *MRS Bull.* **2018**, *43*, 676−682.
(79) Ong, S. P.; Richards, W. D.; Jain, A.; Hautier, G.; Kocher, M.; Cholia, S.; Gunter, D.; Chevrier, V. L.; Persson, K. A.; Ceder, G. Python Materials Genomics (Pymatgen): A Robust, Open-Source Python Library for Materials Analysis. *Comput. Mater. Sci.* **2013**, *68*, 314−319.
(80) Pinsky, M.; Avnir, D. Continuous Symmetry Measures. 5. The Classical Polyhedra. *Inorg. Chem.* **1998**, *37*, 5575−5582.
(81) Giannozzi, P.; Andreussi, O.; Brumme, T.; Bunau, O.; Buongiorno Nardelli, M.; Calandra, M.; Car, R.; Cavazzoni, C.; Ceresoli, D.; Cococcioni, M.; et al. Advanced Capabilities for Materials Modelling with Quantum ESPRESSO. *J. Phys.: Condens. Matter* **2017**, *29*, 465901.
(82) Hamann, D. R. Optimized Norm-Conserving Vanderbilt Pseudopotentials. *Phys. Rev. B: Condens. Matter Mater. Phys.* **2013**, *88*, 085117.
(83) Yu, C.-J. Advances in Modelling and Simulation of Halide Perovskites for Solar Cell Applications. *J. Phys.: Energy* **2019**, *1*, 022001.
(84) Otero-de-la-Roza, A.; Johnson, E. R.; Luaña, V. Critic2: A program for real-space analysis of quantum chemical interactions in solids. *Comput. Phys. Commun.* **2014**, *185*, 1007−1018.
(85) Varadwaj, A.; Varadwaj, P. R.; Marques, H. M.; Yamashita, K. Halogen in Materials Design: Revealing the Nature of Hydrogen Bonding and Other Non-Covalent Interactions in the Polymorphic Transformations of Methylammonium Lead Tribromide Perovskite. *Mater. Today Chem.* **2018**, *9*, 1−16.
(86) Ouyang, R.; Ahmetcik, E.; Carbogno, C.; Scheffler, M.; Ghiringhelli, L. M. Simultaneous Learning of Several Materials Properties from Incomplete Databases with Multi-Task SISSO. *J. Phys.: Mater.* **2019**, *2*, 024002.
(87) Kieslich, G.; Sun, S.; Cheetham, A. K. An extended Tolerance Factor approach for organic-inorganic perovskites. *Chem. Sci.* **2015**, *6*, 3430−3433.
(88) Xie, S. R.; Kotlarz, P.; Hennig, R. G.; Nino, J. C. Machine Learning of Octahedral Tilting in Oxide Perovskites by Symbolic Classification with Compressed Sensing. *Comput. Mater. Sci.* **2020**, *180*, 109690.
(89) Kieslich, G.; Sun, S.; Cheetham, A. K. Solid-state principles applied to organic-inorganic perovskites: new tricks for an old dog. *Chem. Sci.* **2014**, *5*, 4712−4715.
(90) Lu, S.; Zhou, Q.; Ouyang, Y.; Guo, Y.; Li, Q.; Wang, J. Accelerated Discovery of Stable Lead-Free Hybrid Organic-Inorganic Perovskites *via* Machine Learning. *Nat. Commun.* **2018**, *9*, 3405.
(91) El-Mellouhi, F.; Marzouk, A.; Bentria, E. T.; Rashkeev, S. N.; Kais, S.; Alharbi, F. H. Hydrogen Bonding and Stability of Hybrid Organic-Inorganic Perovskites. *ChemSusChem* **2016**, *9*, 2648−2655.
(92) Brammer, L.; Bruton, E. A.; Sherwood, P. Understanding the Behavior of Halogens as Hydrogen Bond Acceptors. *Cryst. Growth Des.* **2001**, *1*, 277−290.
(93) Kovács, A.; Varga, Z. Halogen Acceptors in Hydrogen Bonding. *Coord. Chem. Rev.* **2006**, *250*, 710−727 17th Main Group Chemistry.
(94) Kőrbel, S.; Marques, M. A. L.; Botti, S. Stable Hybrid Organic−Inorganic Halide Perovskites for Photovoltaics from *Ab Initio* High-Throughput Calculations. *J. Mater. Chem. A* **2018**, *6*, 6463−6475.
(95) Greenwood, N.; Earnshaw, A. *Chemistry of the Elements*, 2nd ed.; Butterworth-Heinemann: Oxford, 1997; pp 367−405.
(96) Lee, S.-W.; Kim, S.; Bae, S.; Cho, K.; Chung, T.; Mundt, L. E.; Lee, S.; Park, S.; Park, H.; Schubert, M. C.; et al. UV Degradation and Recovery of Perovskite Solar Cells. *Sci. Rep.* **2016**, *6*, 38150.
(97) Wang, M.; Vasudevan, V.; Lin, S.; Jasieniak, J.; Russo, S. P.; Birbilis, N.; Medhekar, N. V. Molecular Mechanisms of Thermal Instability in Hybrid Perovskite Light Absorbers for Photovoltaic Solar Cells. *J. Mater. Chem. A* **2020**, *8*, 17765−17779.
(98) Goldschmidt, V. M. Krystallbau Und Chemische Zusammensetzung. *Ber. Dtsch. Chem. Ges.* **1927**, *60*, 1263−1296.
(99) Bartel, C. J.; Sutton, C.; Goldsmith, B. R.; Ouyang, R.; Musgrave, C. B.; Ghiringhelli, L. M.; Scheffler, M. New Tolerance Factor to Predict the Stability of Perovskite Oxides and Halides. *Sci. Adv.* **2019**, *5*, No. eaav0693.
(100) Burger, S.; Ehrenreich, M. G.; Kieslich, G. Tolerance factors of hybrid organic-inorganic perovskites: recent improvements and current state of research. *J. Mater. Chem. A* **2018**, *6*, 21785−21793.
(101) Li, C.; Lu, X.; Ding, W.; Feng, L.; Gao, Y.; Guo, Z. Formability of ABX_3 (X = F, Cl, Br, I) Halide Perovskites. *Acta Crystallogr., Sect. B: Struct. Sci.* **2008**, *64*, 702−707.
(102) Bernasconi, A.; Page, K.; Dai, Z.; Tan, L. Z.; Rappe, A. M.; Malavasi, L. Ubiquitous Short-Range Distortion of Hybrid Perovskites and Hydrogen-Bonding Role: the $MAPbCl_3$ Case. *J. Phys. Chem. C* **2018**, *122*, 28265−28272.
(103) Wu, T.; Wang, J. Global Discovery of Stable and Non-Toxic Hybrid Organic-Inorganic Perovskites for Photovoltaic Systems by Combining Machine Learning Method with First Principle Calculations. *Nano Energy* **2019**, *66*, 104070.
(104) Pilania, G.; Balachandran, P. V.; Kim, C.; Lookman, T. Finding New Perovskite Halides via Machine Learning. *Front. Mater.* **2016**, *3*, 19.